FULL PAPER

A Versatile Fluoro-Containing Low-Bandgap Polymer for Efficient Semitransparent and Tandem Polymer Solar Cells

Chih-Yu Chang, Lijian Zuo, Hin-Lap Yip, Yongxi Li, Chang-Zhi Li, Chain-Shu Hsu,* Yen-Ju Cheng, Hongzheng Chen,* Alex K.-Y. Jen*

The versatility of a fluoro-containing low band-gap polymer, poly[2,6-(4,4-bis(2-ethylhexyl)-4H-cyclopenta[2,1-b;3,4-b']dithiophene)-alt-4,7-(5-fluoro-2,1,3-benzothia-diazole)] (PCPDTFBT) in organic photovoltaics (OPVs) applications is demonstrated. High boiling point 1,3,5-trichlorobenzene (TCB) is used as a solvent to manipulate PCPDTFBT:[6,6]-phenyl-C$_{71}$-butyric acid methyl ester (PC$_{71}$BM) active layer morphology to obtain high-performance single-junction devices. It promotes the crystallization of PCPDTFBT polymer, thus improving the charge-transport properties of the active layer. By combining the morphological manipulation with interfacial optimization and device engineering, the single-junction device exhibits both good air stability and high power-conversion efficiency (PCE, of 6.6%). This represents one of the highest PCE values for cyclopenta[2,1-b;3,4-b']dithiophene (CPDT)-based OPVs. This polymer is also utilized for constructing semitransparent solar cells and double-junction tandem solar cells to demonstrate high PCEs of 5.0% and 8.2%, respectively.

1. Introduction

Organic photovoltaics (OPVs) have drawn considerable attention as an economically viable source of renewable energy because of their potential for cost-effective manufacturing, light-weight, and mechanical flexibility.[1–4] So far, bulk hetero-junction (BHJ) OPVs based on conjugated polymers as electron-donor blended with [6,6]-phenyl-C$_{71}$-butyric acid methyl ester (PC$_{71}$BM) as an electron-acceptor have reached high PCE of over 10%,[5] due to significant progress made in exploiting new materials (e.g. low band-gap (LBG) polymers and fullerene bis-adducts),[3,6–10] optimization of BHJ morphology through various treatments (e.g., slow growth and processing additive),[6,11,12] improvement of interface characteristics through interfacial modifications,[13–15] and development of device architectures (e.g. inverted structure and tandem structure).[5,13–19] Development of LBG polymers with absorption characteristics that extend into the near-infrared region has drawn intense attention because of the following reasons: (1) They can potential increase the light harvesting ability and thus photocurrent generation of OPVs;[3] (2) They can be combined with a large band-gap polymer in tandem cells to realize complementary absorption;[5,17,18] (3) They can be used in a semitransparent OPV that strongly absorbs the light from near-infrared region while allowing most of the visible light to get through.[20,21]

A straightforward strategy to reduce polymer band-gap is to incorporate both electron-rich and electron-deficient moieties in the conjugated backbone.[3] One of the representative LBG polymers is poly[4,4-bis(2-ethylhexyl)-4H-cyclopenta[2,1-b;3,4-b']dithiophene-2,6-diyl-alt-2,1,3-benzothiadiazole-4,7-diyl] (PCPDTBT),[6] which combines the electron-rich cyclopenta[2,1-b;3,4-b']dithiophene (CPDT) building block with the electron-deficient 2,1,3-benzothiadiazole-4,7-diyl (BT) unit. The BHJ devices based on PCPDTFBT:PC$_{71}$BM showed a moderate PCE of 5.5%, which is predominantly limited by the low V_{oc} value (0.62 V) due to the high-lying highest occupied molecular orbital (HOMO) level of the polymer.[6] The introduction of a strong electron-withdrawing fluoro atom to the electron-deficient unit of polymer has been proven to be effective in lowering the HOMO level of polymer, resulting in increased V_{oc}.[22–26] Moreover, such F-containing polymers can also possess superior hole mobility and preferable morphology as compared with unmodified polymer, leading to the increased J_{sc} and FF.[22–26] Based on this strategy, a F-containing PCPDTBT polymer, poly[2,6-(4,4-bis(2-ethylhexyl)-4H-cyclopenta[2,1-b;3,4-b']dithiophene)-alt-4,7-(5-fluoro-2,1,3-benzothiadiazole)] (PCPDTFBT, chemical structure shown in **Figure 1**a), has been developed.[24,25]

Dr. C.-Y. Chang, L. Zuo, Dr. H.-L. Yip, Y.-X. Li,
Dr. C.-Z. Li, Prof. A. K.-Y. Jen
Department of Materials Science and Engineering
University of Washington
Seattle, USA
E-mail: ajen@u.washington.edu
Dr. C.-Y. Chang, Prof. C.-S. Hsu, Prof. Y.-J. Cheng
Department of Applied Chemistry
National Chiao Tung University
1001 Ta Hseuh Road, Hsin-Chu, 30010, Taiwan
E-mail: cshsu@mail.nctu.edu.tw
L. Zuo, Prof. H. Z. Chen
State Key Laboratory of Silicon Materials
MOE Key Laboratory of Macromolecule
Synthesis and Functionalization
Zhejiang-California International Nanosystems Institute
Zhejiang University
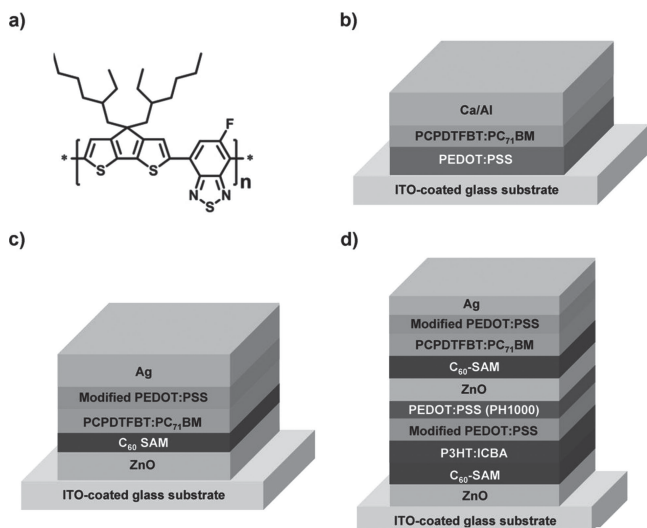Hangzhou, 310027, PR China
E-mail: hzchen@zju.edu.cn

Figure 1. (a) Chemical structure of PCPDTFBT. Schematic representation of the device architecture used in this study: (b) conventional single-junction solar cell, (c) inverted single-junction solar cell and (d) double-junction tandem solar cell.
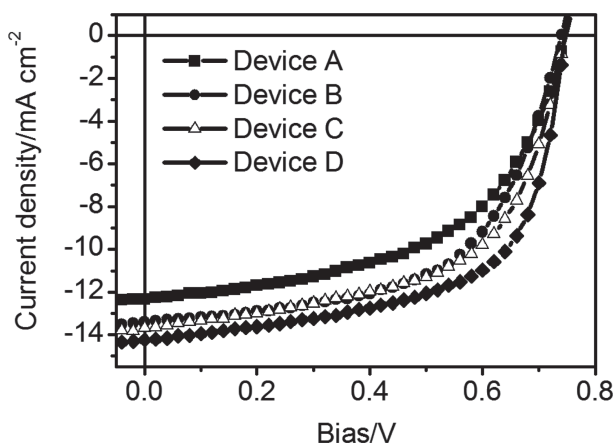

Figure 2. J-V characteristics of the as-fabricated devices (see Table 1 for descriptions of the device types).

By adding 1% 1,8-diiodooctane (DIO) as the processing additive to the processing solvent to manipulate the active layer morphology, the PCE of the device has been increased to 6.16%.[25] The DIO is suggested to promote the formation of PCPDFTBT fibrils due to its low vapor pressure (and therefore prolonged evaporation time) and preferential solubility for $PC_{71}BM$, leading to the formation of interpenetrating bi-continuous network within a BHJ film.[25]

In this work, we demonstrate the versatility of PCPDTFBT for OPVs, including the application of it for single-junction solar cells, semitransparent solar cells, and double-junction tandem solar cells. To achieve high performance single-junction cells, 1,3,5-trichlorobenzene (TCB) was used as the solvent to manipulate PCPDTFBT:$PC_{71}BM$ morphology without using any processing additives. The high boiling point TCB prolongs the solvent evaporation time and promotes the crystallization of BHJ film, leading to increased hole mobility and balanced charge transport. By combining the morphological manipulation with interface optimization and device engineering, the single-junction cell exhibits both high PCE (6.6%) and excellent air stability. More importantly, PCPDTFBT can be used to demonstrate highly-efficient semitransparent solar cells (PCE = 5.0%, average visible transmittance (AVT) = 47.3%) and double-junction tandem solar cells (PCE = 8.2%).

2. Results and Discussion

2.1. Conventional Single-Junction Solar Cells

Initially, we investigated the solvent effect on the performance of PCPDTFBT:$PC_{71}BM$-based single-junction solar cell, with a conventional structure of indium tin oxide (ITO)-coated glass/poly(3,4-ethylenedioxythiophene):poly(styrenesulfonate) (PEDOT:PSS)/active layer/Ca/Al (Figure 1b). Two solvents were examined herein: ortho-dichlorobenzene (ODCB) and TCB. The current–voltage (J-V) characteristics of the devices were shown in **Figure 2**, and the corresponding device parameters were summarized in **Table 1**. The ODCB-processed device (Device A) exhibited a short-circuit current density (J_{sc}) of 12.35 mA cm^{-2}, an open-circuit voltage (V_{oc}) of 0.74 V, and a fill factor (FF) of 54.19%, with a PCE of 5.0%, while the TCB-processed device (Device B) showed a relative high PCE of 5.8%, with a J_{sc} of 13.43 mA cm^{-2}, an V_{oc} of 0.74 V, and a FF of 58.05%. Although both ODCB and TCB are good solvents for PCPDTFBT (solubility > 20 mg mL^{-1}), their difference in boiling point (ca. 181 °C for ODCB and ca. 208 °C for TCB) can largely influence the absorption characteristics, crystallinity and morphology of PCPDTFBT:$PC_{71}BM$ BHJ films.

Compared with the UV–vis absorption spectrum of ODCB-cast film, a slight red-shift peak at the long wavelength region (>650 nm) and a clear vibronic shoulder at 790 nm were

Table 1. Summary of the photovoltaic device parameters for the single-junction devices.

Device	Conditions[a]	V_{oc} [V]	J_{sc} [mA cm^{-2}]	FF [%]	PCE [%]	μ_h[d] [cm^2 V^{-1} s^{-1}]	μ_e[d] [cm^2 V^{-1} s^{-1}]
A	Conventional, ODCB	0.74	12.35	54.19	5.0	3.1×10^{-4}	2.2×10^{-3}
B	Conventional, TCB	0.74	13.43	58.05	5.8	2.6×10^{-3}	1.5×10^{-3}
C	Inverted, TCB	0.75	13.70	57.79	6.0	-	-
D	Inverted, TCB[b]	0.74	14.24 (13.95)[c]	61.68	6.6	-	-

[a]Device architecture, solvent; [b]With C_{60}–SAM layer; [c]Calculated from the IPCE spectra shown in Figure 6; [d]Estimated by SCLC model.

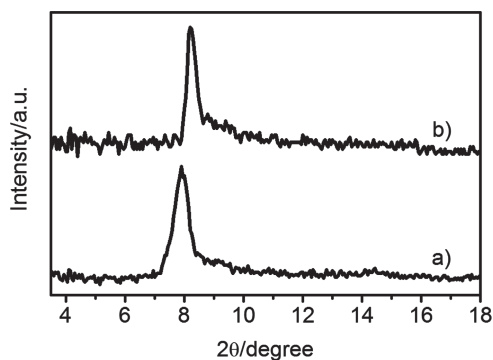**Figure 3.** XRD patterns of PCPDTFBT films cast from: (a) ODCB and (b) TCB.

Table 2. Calculated d-spacing and size of crystallites for PCPDTFBT films cast from ODCB and TCB.

Solvent	d-spacing[a] [nm]	Size of crystallites[b] [nm]
ODCB	1.12	14.61
TCB	1.07	20.69

[a]Determined by Bragg's equation; [b]Determined by Scherrer's equation.

observed in the TCB-cast film (Figure S1a), which can be ascribed to stronger interchain interaction and higher ordering of PCPDTFBT. This distinction is more evident in UV-Vis absorption spectra of pure PCPDTFBT films (Figure S1b). To gain more insights into the solvent effect on the microstructure of PCPDTFBT films, X-ray diffraction (XRD) analysis was performed. As shown in **Figure 3**, ODCB- and TCB-cast films exhibited a strong diffraction peak at 2θ value of 7.87° and 8.23°, respectively, corresponding to the (100) reflection of the lamella structure of PCPDTFBT. The solvent-induced change in the diffraction peak position shown in Figure 3 is consistent with previous studies and may result from the self-annealing of crystal defects.[27,28] The lamellar d-spacing and crystallite size of PCPDTFBT can be obtained from the information of (100) peak using the Bragg's and Scherrer's equation,[29] respectively. As shown in **Table 2**, compared with ODCB-cast film, TCB-cast film exhibited a slightly smaller lamellar d-spacing (1.07 nm vs. 1.12 nm) and a larger grain size of crystallites (20.69 nm vs. 14.61 nm). These results are in good agreement with the results obtained by UV absorption spectra (Figure S1) and also provide further insights into effective charge transport of TCB-processed film, as discussed below.

The difference in the crystallization between ODCB- and TCB-cast BHJ films was also manifested in the atomic force microscopy (AFM) images (**Figure 4**): The film cast from TCB exhibited a rougher surface and better defined crystallite fibrils structure than the film cast from ODCB. The root-mean-square (rms) roughnesses are 2.28 and 1.16 nm for TCB- and ODCB-cast films, respectively. To further understand the solvent effect on the charge- transporting properties of the BHJ film, both electron- and hole-only devices were fabricated to estimate charge mobility by the space charge limited current (SCLC) model.

As shown in Table 1 and Figure S2, the TCB-cast film exhibited an increased hole mobility (μ_h) by almost one order of

magnitude (from 3.1×10^{-4} cm^2 V^{-1} s^{-1} to 2.6×10^{-3} cm^2 V^{-1} s^{-1}) while the electron mobility (μ_e) of the devices remained essentially unchanged (ca. 1.8×10^{-3} cm^2 V^{-1} s^{-1}), leading to the more balance electron/hole mobilities that can effectively reduce space charge build-up within the active layer.[11,30] In view of increased molecular ordering, optimized morphology and enhanced hole mobility, we suggest that high boiling point TCB prolongs the evaporation time to facilitate the self-organization of PCPDTFBT into an optimal morphology, and thus improving device performance.

2.2. Inverted Single-Junction Solar Cells

The inverted structure device have been considered as a potential alternative to achieve higher performance and stability compared to the conventional one due to the removal of susceptible low-work-function metals,[16] preferable vertical phase separation,[31] and favorable distribution of optical field in the inverted device.[32] On the basis of the above reasons, we have evaluated the performance of PCPDTFBT:PC$_{71}$BM-based single-junction
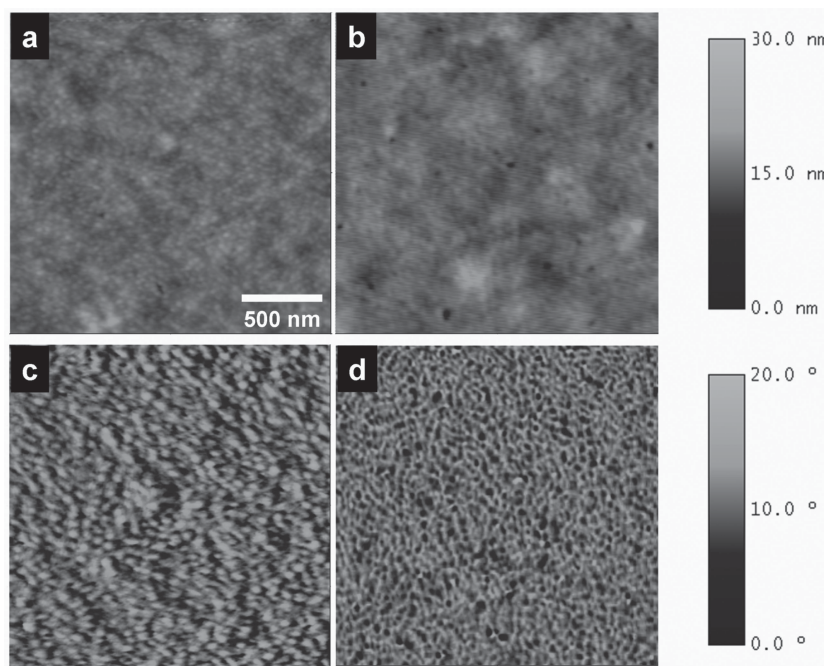

Figure 4. AFM topography (top) and phase (bottom) images of PCPDTFBT:PC$_{71}$BM films cast from ODCB (a,c) and TCB (b,d). The rms roughness of ODCB- and TCB-cast films is 1.16 nm and 2.28 nm, respectively. The scan size is 2 μm × 2 μm.
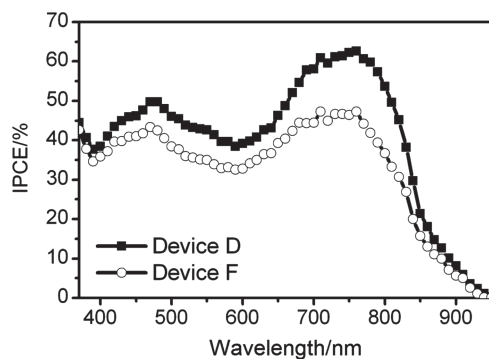
www.MaterialsViews.com

ADVANCED
FUNCTIONAL
MATERIALS
www.afm-journal.de

FULL PAPER

Figure 5. IPCE spectra of the as-fabricated devices (see Table 1 and Table 3 for descriptions of the device types).

Table 3. Summary of the photovoltaic device parameters for the semi-transparent cells.

Device	Ag thickness [nm]	V_{oc} [V]	J_{sc} [mA cm^{-2}]	FF [%]	PCE [%]	AVT[b] [%]
E	15	0.73	11.90	58.34	5.1	39.4
F	10	0.74	11.39 (10.93)[a]	58.56	5.0	47.3

[a]Calculated from the IPCE spectra shown in Figure 6; [b]Wavelength range: 380–700 nm.

device with the inverted structure (ITO-coated glass/ZnO/active layer/modified PEDOT:PSS/Ag). The inverted device (device C) exhibited a J_{sc} of 13.70 mA cm^{-2}, an V_{oc} of 0.75 V, a FF of 57.79%, and a PCE of 6.0% (Table 1 and Figure 2). By inserting a fullerene self-assembled monolayer (C$_{60}$-SAM) at the interface between ZnO and the active layer (device D; device structure is shown in Figure 1c), the PCE can be further increased to 6.6%, with a J_{sc} of 14.24 mA cm^{-2}, an V_{oc} of 0.74 V, and a FF of 61.68% (Table 1 and Figure 2). The J_{sc} value of Device D is in good agreement with the values calculated from integrated incident photon-to-current conversion efficiency (IPCE) spectra (Table 1 and **Figure 5**), which confirms the accuracy of the reported PCE value. It is worth noting that 6.6% represents one of the highest PCE for CPDT-based OPV devices.

The improved PCE obtained from the C$_{60}$-SAM modified cell is consistent with our previous findings and can be attributed to the passivation of surface traps of ZnO and the enhancement of electronic coupling at the ZnO/active layer interface.[13,14] The effectiveness of the C$_{60}$-SAM modification is also manifested in increased shunt resistance (i.e. reduced leakage current) and reduced series resistance (i.e. improved charge carrier extraction) of device D compared to those of device C (Table S1 and Figure S3). In addition, the PCE of inverted device D is superior to that of conventional device B (6.6% vs. 5.8%; Table 1), indicating the PCPDTFBT:PC$_{71}$BM BHJ system is ideal for use in the inverted structure.

More importantly, without encapsulation, device D also possesses good air stability: more than 80% of the initial PCE was retained after more than 2000 h of storage in ambient air (Figure S4; PCE = 5.9%, with a J_{sc} of 12.42 mA cm^{-2}, an V_{oc} of 0.74 V, and a FF of 58.05%). We suggest that this superior air stability may be associated with the low-lying HOMO level of PCPDTFBT afforded by the stronger FBT electron-withdrawing strength.

2.3. Semitransparent Solar Cells

Semitransparent solar cells have great potential to be used in many photovoltaic applications, such as power-generating windows for buildings and automotives.[33–35] Considering the major absorption of PCPDTFBT locates at the near infrared region and most of the visible light is unutilized (Figure 3b), it would be ideal for making semitransparent solar cells.

Therefore, we have also applied PCPDTFBT:PC$_{71}$BM as active BHJ layer in semitransparent solar cell, with a configuration of ITO/ZnO/active layer/PEDOT:PSS/ultra-thin Ag (thickness = 10 or 15 nm). With a 15 nm Ag as the semitransparent top electrode, device E exhibited a reasonable PCE of 5.1% (**Table 3** and **Figure 6**) with a moderate AVT of 39.4% (**Figure 7**). Interestingly, for device with thinner Ag layer of 10 nm (device F), the AVT can be increased to 47.3% (Figure 7) without compromising its PCE significantly (5.0%; Table 3 and Figure 6), which represents the highest value reported for semitransparent cells with similar transparency. This finding is associated with the good wettability of Ag atoms on the polar PEDOT:PSS layer, which allows Ag atoms to grow homogeneously via Stranski–Krastanov growth model.[36] The
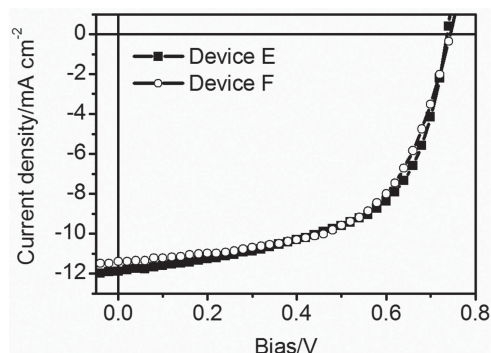

Figure 6. J–V characteristics of the as-fabricated devices (see Table 3 for descriptions of the device types).
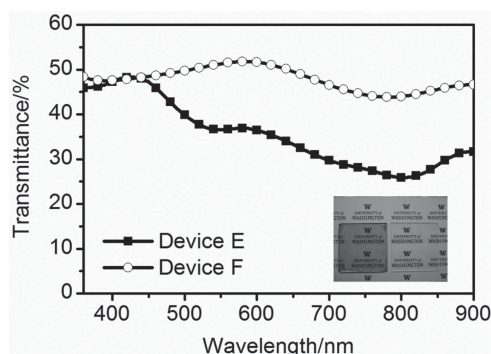

Figure 7. Optical transmittance of the as-fabricated devices (see Table 3 for descriptions of the device types). The inset shows a photograph of device F and a bare ITO-coated glass.

FULL PAPER

effectiveness of PEDOT:PSS seed layer was manifested in more homogeneous morphology with lower rms surface roughness (Figure S5), lower sheet resistance (Table S2), and higher AVT (Figure S6) of 10-nm Ag-coated PEDOT:PSS films compared with those of Ag films deposited without the PEDOT:PSS layer. The photographic image of device F was also shown in inset of Figure 7, where the University of Washington logo can be visualized clearly through the device.

2.4. Tandem Soar Cells

Stacking two individual sub-cells with complementary absorption profiles into the tandem architecture has been proven as an effective way to harvest broader range of the solar spectrum and minimize the thermalization loss of photon energy to improve the device performance.[5,17–19] Here, a double-junction tandem solar cell consisting of a front cell with poly(3-hexylthiophene) (P3HT):indene-C_{60} bisadduct (ICBA) wide-bandgap material (ca. 1.85 eV) and a rear cell with PCPDTFBT:$PC_{71}BM$ LBG material (ca. 1.37 eV) is studied, and the device structure is illustrated in Figure 1d. The two sub-cells are connected in series through an interconnection layer (ICL) comprising modified-PEDOT:PSS/high conductivity PEDOT:PSS (hereafter referred to as PH1000)/ZnO films. This ICL possesses desired properties, including a high optical transparency of ~85% in the 700–900 nm range (Figure S7), a reasonable conductivity of ca. 15 S cm^{-1}, a smooth surface (an rms roughness of 0.88 nm; Figure S8), and an excellent robustness against subsequent TCB solvent as evidenced by the nearly identical UV-Vis spectra of P3HT:ICBA films before and after rinsing with TCB (Figure S9).

Very encouragingly, the resulting tandem cell showed a J_{sc} of 7.83 mA cm^{-2}, an V_{oc} of 1.57 V, and a FF of 66.46%, and a high PCE of 8.2%, which is higher than that of each sub-cell (**Table 4** and **Figure 8**). The IPCE spectrum of the tandem cell without light bias exhibited a broad spectral response range from UV to near-IR region (Figure S10), indicating that each sub-cell works individually. In addition, the V_{oc} of the tandem cell is equal to the sum of V_{oc} of the each sub-cell (Table 4 and Figure 8), confirming the effectiveness of the ICL. These results clearly indicate the feasibility of using PCPDTFBT LBG polymer for the development of highly efficient tandem solar cells.

3. Conclusions

We have demonstrated the versatility of a fluoro-containing LBG polymer PCPDTFBT in diverse photovoltaic applications.

Table 4. Summary of the photovoltaic device parameters for the sub-cells and tandem cell.

Device	V_{oc} [V]	J_{sc} [mA cm^{-2}]	FF [%]	PCE [%]
Front cell	0.83	11.59 (10.86)[a]	68.05	6.5
Rear cell	0.74	14.24 (13.95)[b]	61.68	6.6
Tandem cell	1.57	7.83	66.46	8.2

[a]Calculated from the IPCE spectra shown in Figure 6; [b]Calculated from the IPCE spectra shown in Figure S11.
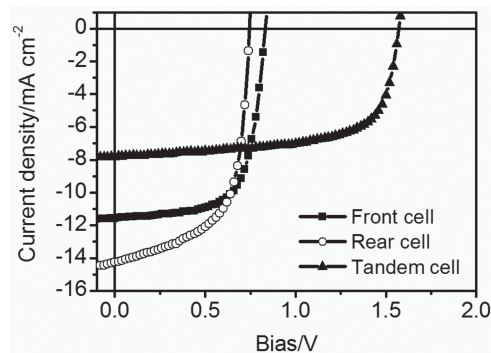

Figure 8. J–V characteristics of the sub-cells and tandem cell.

By combining morphological, interface and device engineering, the single-junction cell showed both a record high PCE (6.6%) for the CPDT-based OPVs and good air stability. In addition, the semitransparent cell showed a high PCE of 5.0% with an AVT of 47.3%, which represents the highest value reported for semi-transparent cells with similar transparency. More importantly, the double-junction tandem cell based on using P3HT:ICBA and PCPDTFBT:$PC_{71}BM$ active layers exhibited a high PCE of 8.2%. These encouraging results show that PCPDTFBT can be a very promising LBG polymer for diverse applications in OPVs.

4. Experimental Section

Materials: PCPDTFBT was synthesized in house, and the detailed synthesis can be found elsewhere.[23] The number average molecular weight of PCPDTFBT is ~25.3 kDa with a polydispersity index of 1.5, as determined by gel permeation chromatography. P3HT was purchased from Rieke Metals, ICBA was purchased from Lumtec, and $PC_{71}BM$ was purchased from American Dye Source. Unless otherwise stated, all chemicals were purchased from Aldrich and used as received.

Single-Junction Cell Fabrication: The device architecture of the conventional single-junction solar cell is shown in Figure 1b. ITO-coated glass substrates (15 Ω cm^{-2}) were cleaned stepwise in detergent, water, acetone, and isopropyl alcohol under ultrasonication for 20 min each and subsequently pretreated by air plasma for 30 min. A PEDOT:PSS layer (Baytron P VP A1 4083) was spin-coated onto the ITO surface. After annealing at 140 °C for 20 min in air, the substrates were transferred into an N_2-filled glovebox. The active layer (ca. 100 nm) was then spin-cast from the blend solutions of 8 mg mL^{-1} PCPDTFBT and 20 mg mL^{-1} $PC_{71}BM$ in either ODCB or TCB, followed by annealing at 120 °C for 10 min. A Ca layer (20 nm) and an Al layer (100 nm) were then deposited under high vacuum (<10^{-6} torr) through a shadow mask, which defined an active area of 0.036 cm^2.

The device architecture of the inverted single-junction solar cell is shown in Figure 1c. A ZnO precursor solution, consisting of 20 mg mL^{-1} zinc acetylacetonate hydrate in anhydrous ethanol, was spin-coated onto cleaned ITO-coated glass, followed by thermal annealing in air at 130 °C for 5 min (ca. 20 nm). Subsequently, a C_{60}-SAM layer was deposited on ZnO using a spin-coating process as previously reported.[14] The substrates were washed with THF twice to remove unbound C_{60}-SAM molecules. The same procedure for the active layer in the conventional device was used for the inverted devices. The modified PEDOT:PSS layer (ca. 70 nm) was then spin-coated from PEDOT:PSS solution (Clevious P VP A1 4083) diluted with equal volume of isopropyl alcohol and 0.2 wt% of Zonyl FSO fluorosurfactant. Afterward, an Ag layer (150 nm) was then deposited under high vacuum (<10^{-6} torr) through a shadow mask, which defined an active area of 0.036 cm^2. Finally, the complete device was thermally annealed at 140 °C for 5 min.

Semitransparent Cell Fabrication: The fabrication procedure was the same as that used for the inverted solar cells, except that Ag thickness was controlled to be 10 or 15 nm.

Tandem Cell Fabrication: The device architecture of the tandem solar cell is shown in Figure 1d. ITO-coated glass substrates (15 Ω cm^{-2}) were cleaned stepwise in detergent, water, acetone, and isopropyl alcohol under ultrasonication for 20 min each and subsequently pretreated by air plasma for 30 min. A ZnO precursor solution, consisting of 20 mg mL^{-1} zinc acetylacetonate hydrate in anhydrous ethanol, was spin-coated onto cleaned ITO-coated glass, followed by thermal annealing in air at 130 °C for 5 min (ca. 20 nm). Subsequently, a C$_{60}$-SAM layer was deposited on ZnO using a spin-coating process as previously reported.[14] The substrates were washed with THF twice to remove unbound C$_{60}$-SAM molecules.

The active layer of the bottom cell (ca. 150 nm) was then spin-coated from the blend solutions of 17 mg mL^{-1} P3HT and 17 mg mL^{-1} ICBA in ODCB, followed by drying the films at room temperature overnight in a closed Petri dish. The modified PEDOT:PSS layer (ca. 80 nm) was then spin-coated from the PEDOT:PSS solution (Clevious P VP A1 4083) diluted with equal volume of isopropyl alcohol and 0.2 wt% of Zonyl FSO fluorosurfactant. After being annealed at 120 °C for 5 min, PH1000 layer (ca. 40 nm) was spin-coated from its solution (Clevious PH1000) and then annealed at 120 °C for 5 min. The surface of the PH1000 layer was then washed with methanol to increase the conductivity and reduce the surface roughness as reported elsewhere.[37] It should be noted that PH1000 layer used herein can ensure the ohmic contact between the modified PEDOT:PSS and ZnO layers. The device without PH1000 layer usually exhibits a S-shaped kink in the J-V characteristics and therefore a deteriorated PCE.

The same procedure for ZnO/C$_{60}$-SAM layers in the bottom cell was used for the top cell. After that, the active layer (ca. 100 nm) of the top cell was then spin-coated from the blend solutions of 8 mg mL^{-1} PCPDTFBT and 20 mg mL^{-1} PC$_{71}$BM in TCB. The modified PEDOT:PSS layer (ca. 70 nm) was then spin-coated from its solution (Clevious P VP A1 4083) diluted with equal volume of isopropyl alcohol and 0.2 wt% of Zonyl FSO fluorosurfactant. Afterward, an Ag layer (250 nm) was then deposited under high vacuum (<10^{-6} torr) through a shadow mask which defined an active area of 0.036 cm^2. Finally, the complete device was thermally annealed at 140 °C for 5 min.

SCLC Mobility Measurement: The single-carrier mobility can be extracted from the dark J–V characteristics of the hole-only and electron-only devices by using SCLC model:[26,38]

$$J = \frac{9}{8}\varepsilon_0\varepsilon_r\mu \, \exp\left(0.891\gamma\sqrt{\frac{V}{L}}\right)\frac{V^2}{L^3}$$

Where ε_0 is the permittivity of free space, ε_r is the relative permittivity of the material, μ is the charge carrier mobility, γ is the field activation factor, and L is the thickness of the active layer. The hole-only device was constructed as ITO/PEDOT:PSS (40 nm)/PCPDTFBT: PC$_{71}$BM (100 nm)/MoO$_3$ (10 nm)/Ag (100 nm), and the electron-only device was constructed as ITO/Al (100 nm)/PCPDTFBT:PC$_{71}$BM (100 nm)/Ca (20 nm)/Al (100 nm). The fabrication procedure was identical to that of solar cell fabrication except for the electrodes.

Characterization: The current-voltage characteristics of unencapsulated solar cell devices were measured under ambient using a Keithley 2400 source-measurement unit. An Oriel xenon lamp (450 Watt) with an AM1.5 G filter was used as the solar simulator. Contributions to the J$_{sc}$ from regions outside the active area were eliminated using illumination masks with aperture size of 0.0314 cm^2. A Hamamatsu silicon solar cell with a KG5 color filter, which is traced to the National Renewable Energy Laboratory (NREL), was used as the reference cell. To calibrate the light intensity of the solar simulator, the power of the xenon lamp was adjusted to make the J$_{SC}$ of the reference cell under simulated sun light as high as it was under the calibration condition. The spectral mismatches resulting from the test cells, the reference cell, the solar simulator, and the AM1.5 were calibrated with mismatch factors (M). According to Shrotriya et al.,[39] the mismatch factor is defined as

$$M = \frac{\int_{\lambda 1}^{\lambda 2} E_{Ref}(\lambda)S_R(\lambda)d\lambda \int_{\lambda 1}^{\lambda 2} E_S(\lambda)S_T(\lambda)d\lambda}{\int_{\lambda 1}^{\lambda 2} E_{Ref}(\lambda)S_T(\lambda)d\lambda \int_{\lambda 1}^{\lambda 2} E_s(\lambda)S_R(\lambda)d\lambda}$$

where $E_{Ref}(\lambda)$ is the reference spectral irradiance (AM1.5), $E_S(\lambda)$ is the source spectral irradiance, $S_R(\lambda)$ is the spectral responsivity of the reference cell, and $S_T(\lambda)$ is the spectral responsivity of the test cell, each as a function of wavelength (λ). The spectral responsivities of the test cells and the reference cell were calculated from the corresponding external quantum efficiencies (EQE) by the relationship

$$S(\lambda) = \frac{q\lambda}{hc}EQE(\lambda)$$

where the constant term q/hc equals 8.0655 × 10^5 for wavelength in units of meters and $S(\lambda)$ in units of AW^{-1}. The Hamamatsu solar cell was also used as the detector for determining the spectral irradiance of the solar simulator. To minimize the spectral transformation, the irradiance spectrum has been calibrated with the spectral responsively of the Hamamatsu cell and the grating efficiency curve of the monochromator (Oriel Cornerstone 130). UV-Vis absorption spectra were recorded with Perkin-Elmer Lambda-9 spectrophotometer at room temperature. The surface morphology of the polymer films was studied using the tapping mode AFM from a Veeco Nanoscope III controller. The X-ray diffraction spectra of the thin films were recorded using a D8 DISCOVER (Bruker AXS) as the CuK source (wavelength = 1.541 Å) and an output voltage of 40 kV at 40 mA (1600 W). Sheet resistances of the thin films were measured by using a four point probe setup with a source measurement unit (Keithley 2400).

Supporting Information

Supporting Information is available from the Wiley Online Library or from the author.

Acknowledgements

[1] K. M. Coakley, M. D. McGehee, *Chem. Mater.* **2004**, *16*, 4533.
[2] B. C. Thompson, J. M. J. Fréchet, *Angew. Chem. Int. Ed.* **2008**, *47*, 58.
[3] Y. J. Cheng, S. H. Yang, C. S. Hsu, *Chem. Rev.* **2009**, *109*, 5868.
[4] G. Dennler, M. C. Scharber, C. J. Brabec, *Adv. Mater.* **2009**, *21*, 1323.
[5] J. You, L. Dou, K. Yoshimura, T. Kato, K. Ohya, T. Moriarty, K. Emery, C.-C. Chen, J. Gao, G. Li, Y. Yang, *Nat. Commun.* **2013**, *4*, 1446.
[6] J. Peet, J. Y. Kim, N. E. Coates, W. L. Ma, D. Moses, A. J. Heeger, G. C. Bazan, *Nat. Mater.* **2007**, *6*, 497.
[7] G. Zhao, Y. He, Y. Li, *Adv. Mater.* **2010**, *22*, 4355.
[8] Y. He, H.-Y. Chen, J. Hou, Y. Li, *J. Am. Chem. Soc.* **2010**, *132*, 1377.
[9] Y. Wu, Z. Li, W. Ma, Y. Huang, L. Huo, X. Guo, M. Zhang, H. Ade, J. Hou, *Adv. Mater.* 2013, DOI: 10.1002/adma.201301174.
[10] Y. Huang, X. Guo, F. Liu, L. Huo, Y. Chen, T. P. Russell, C. C. Han, Y. Li, J. Hou, *Adv. Mater.* **2012**, *24*, 3383.
[11] G. Li, V. Shrotriya, J. Huang, Y. Yao, T. Moriarty, K. Emery, Y. Yang, *Nat. Mater.* **2005**, *4*, 864.
[12] J. K. Lee, W. L. Ma, C. J. Brabec, J. Yuen, J. S. Moon, J. Y. Kim, K. Lee, G. C. Bazan, A. J. Heeger, *J. Am. Chem. Soc.* **2008**, *130*, 3619.

[13] S. K. Hau, H.-L. Yip, O. Acton, N. S. Baek, H. Ma, A. K. Y. Jen, *J. Mater. Chem.* **2008**, *18*, 5113.

[14] S. K. Hau, H.-L. Yip, H. Ma, A. K. Y. Jen, *Appl. Phys. Lett.* **2008**, *93*, 233304.

[15] T. Yang, M. Wang, C. Duan, X. Hu, L. Huang, J. Peng, F. Huang, X. Gong, *Energy Environ. Sci.* **2012**, *5*, 8208.

[16] S. K. Hau, H.-L. Yip, N. S. Baek, J. Zou, K. O'Malley, A. K. Y. Jen, *Appl. Phys. Lett.* **2008**, *92*, 253301.

[17] L. Dou, J. You, J. Yang, C.-C. Chen, Y. He, S. Murase, T. Moriarty, K. Emery, G. Li, Y. Yang, *Nat. Photon.* **2012**, *6*, 180.

[18] J. Y. Kim, K. Lee, N. E. Coates, D. Moses, T.-Q. Nguyen, M. Dante, A. J. Heeger, *Science* **2007**, *317*, 222.

[19] S. K. Hau, H.-L. Yip, K.-S. Chen, J. Zou, A. K.-Y. Jen, *Appl. Phys. Lett.* **2010**, *97*, 253307.

[20] L. Dou, W.-H. Chang, J. Gao, C.-C. Chen, J. You, Y. Yang, *Adv. Mater.* **2013**, *25*, 825.

[21] C.-C. Chen, L. Dou, R. Zhu, C.-H. Chung, T.-B. Song, Y. B. Zheng, S. Hawks, G. Li, P. S. Weiss, Y. Yang, *ACS Nano* **2012**, *6*, 7185.

[22] H. Zhou, L. Yang, A. C. Stuart, S. C. Price, S. Liu, W. You, *Angew. Chem. Int. Ed.* **2011**, *50*, 2995.

[23] A. C. Stuart, J. R. Tumbleston, H. Zhou, W. Li, S. Liu, H. Ade, W. You, *J. Am. Chem. Soc.* **2013**, *135*, 1806.

[24] Y. Zhang, J. Zou, C.-C. Cheuh, H.-L. Yip, A. K. Y. Jen, *Macromolecules* **2012**, *45*, 5427.

[25] S. Albrecht, S. Janietz, W. Schindler, J. Frisch, J. Kurpiers, J. Kniepert, S. Inal, P. Pingel, K. Fostiropoulos, N. Koch, D. Neher, *J. Am. Chem. Soc.* **2012**, *134*, 14932.

[26] H. Bronstein, J. M. Frost, A. Hadipour, Y. Kim, C. B. Nielsen, R. S. Ashraf, B. P. Rand, S. Watkins, I. McCulloch, *Chem. Mater.* **2013**, *25*, 277.

[27] T. Wang, A. D. F. Dunbar, P. A. Staniec, A. J. Pearson, P. E. Hopkinson, J. E. MacDonald, S. Lilliu, C. Pizzey, N. J. Terrill, A. M. Donald, A. J. Ryan, R. A. L. Jones, D. G. Lidzey, *Soft Matter* **2010**, *6*, 4128.

[28] C.-W. Chu, H. Yang, W.-J. Hou, J. Huang, G. Li, Y. Yang, *Appl. Phys. Lett.* **2008**, *92*, 103306.

[29] B. D. Cullity, *Elements of X-ray Diffraction*, Addison-Wesley Pub. Co., Reading, Mass, USA **1956**.

[30] V. D. Mihailetchi, H. Xie, B. De Boer, L. J. A. Koster, P. W. M. Blom, *Adv. Funct. Mater.* **2006**, *16*, 699.

[31] Z. Xu, L.-M. Chen, G. Yang, C.-H. Huang, J. Hou, Y. Wu, G. Li, C.-S. Hsu, Y. Yang, *Adv. Funct. Mater.* **2009**, *19*, 1227.

[32] S. Albrecht, S. Schäfer, I. Lange, S. Yilmaz, I. Dumsch, S. Allard, U. Scherf, A. Hertwig, D. Neher, *Org. Electron.* **2012**, *13*, 615.

[33] K.-S. Chen, J.-F. Salinas, H.-L. Yip, L. Huo, J. Hou, A. K. Y. Jen, *Energy Environ. Sci.* **2012**, *5*, 9551.

[34] C.-C. Chueh, S.-C. Chien, H.-L. Yip, J. F. Salinas, C.-Z. Li, K.-S. Chen, F.-C. Chen, W.-C. Chen, A. K. Y. Jen, *Adv. Energy Mater.* **2013**, *3*, 417.

[35] Z. Tang, Z. George, Z. Ma, J. Bergqvist, K. Tvingstedt, K. Vandewal, E. Wang, L. M. Andersson, M. R. Andersson, F. Zhang, O. Inganäs, *Adv. Energy Mater.* **2012**, *2*, 1467.

[36] L. Ke, S. C. Lai, H. Liu, C. K. N. Peh, B. Wang, J. H. Teng, *ACS Appl. Mater. Inter.* **2012**, *4*, 1247.

[37] D. Alemu, H.-Y. Wei, K.-C. Ho, C.-W. Chu, *Energy Environ. Sci.* **2012**, *5*, 9662.

[38] M. F. Falzon, M. M. Wienk, R. A. J. Janssen, *J. Phys. Chem. C* **2011**, *115*, 3178.

[39] V. Shrotriya, G. Li, Y. Yao, T. Moriarty, K. Emery, Y. Yang, *Adv. Funct. Mater.* **2006**, *16*, 2016.